ACS OMEGA

Open Access

http://pubs.acs.org/journal/acsodf

Article

Noncoordinating Anions as Key Modulators of Supramolecular Structures, Optical and Electrical Properties in Nickel(II) Complexes

Subhajit Saha, Samit Pramanik, Sudipta Pathak, Kinsuk Das, Riya Sadhukhan, Arnab Ghosh, Dipak K. Goswami, Hon Man Lee, Joaquín Ortega-Castro, Antonio Frontera,* and Subrata Mukhopadhyay*

Cite This: *ACS Omega* 2024, 9, 44494−44506

Read Online

ACCESS | Metrics & More | Article Recommendations | Supporting Information

ABSTRACT: This study explores the synthesis, structural characterization, and examination of two nickel(II) complexes, $[Ni(\mathbf{N_3L_1})_2](NO_3)_2$ (complex **1**) and $[Ni(\mathbf{N_3L_1})_2](ClO_4)_2$ (complex **2**), using the newly synthesized organic heterocyclic chelating ligand $\mathbf{N_3L_1}$ [4-imidazole-2,6-di(pyrazinyl)pyridine]. Through single-crystal X-ray diffraction, we have detailed the crystal structures of these complexes, highlighting their distorted octahedral geometries and diverse supramolecular interactions including $\pi\cdots\pi$ stacking, anion$\cdots\pi$, and hydrogen bonding. These interactions crucially influence the formation of distinct one- and two-dimensional supramolecular architectures. Density functional theory (DFT) calculations were utilized to probe these noncovalent interactions, revealing insights into their stereoelectronic influence and stability in the solid state. Additionally, the electronic properties of the complexes were explored through their electrical characterizations in Schottky diodes, which suggest the potential of these complexes in Schottky diode based electronic devices applications. Notably, complex **2**, incorporating perchlorate anions, exhibited better electrical properties than complex **1**. This work aims to elucidate the role of noncoordinating counteranions in the structural integrity and photophysical behavior of these complexes, while also providing a structure−function correlation through detailed theoretical analysis.

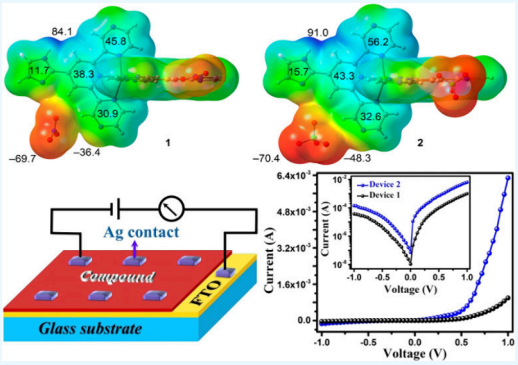

INTRODUCTION

The construction of coordination complexes (CCs) by using the concepts of crystal engineering became a flourishing research field due to their remarkable functional properties with broad applications in the areas of catalysis, gas storage, magnetism, luminescence, and molecular sensing.[1−5] To design such metal−organic networks with intriguing structural types and unusual properties, careful consideration must be given to the nature and multifunctionality of organic building blocks. Crystal Engineering is the scientific discipline that explores how intermolecular interactions contribute to the construction of molecular architectures.[6,7] The formation, growth, and stability of crystals rely on a multitude of noncovalent interactions, including hydrogen bonds, halogen bonds, cation$\cdots\pi$, anion$\cdots\pi$, $\pi\cdots\pi$ stacking, lone pair$\cdots\pi$, and C−H$\cdots\pi$ interactions, which exhibit relatively weaker strengths.[8,9] Comparatively, underappreciation of anion$\cdots\pi$ interaction has relied on the assumption of electrostatic repulsion between two electron rich systems, but in the recent past, such anion$\cdots\pi$ interaction has captured the attention of synthetic chemists as now it is recognized as a potential noncovalent interactions and may play a pivotal role in forming supramolecular architectures. From the available data of the crystallographic database,[10−15] it may be concluded that anion$\cdots\pi$ interactions are not able to stabilize an architecture alone but it needs a synergetic support from either H-boding interactions or $\pi\cdots\pi$ interactions or both. The major challenge is to consider both $\pi\cdots\pi$ and anion$\cdots\pi$ interactions simultaneously as the prime requirements for these two interactions are opposite: anion$\cdots\pi$ interactions become preferred with electron deficient π rings (which may be attained by either ring protonation, presence of electron withdrawing substituents, or metal coordination), where $\pi\cdots\pi$ interactions require electron-rich π systems.

Nitrogen based heterocyclic multidentate ligands remain promising candidates for designing versatile networks using noncovalent interactions.[16−21] The widespread use of 2,2′:6′,2″-terpyridine (tpy) as a prototypical tridentate motif is owed to its exceptional ability to form complexes with various transition metal ions, incorporating their robust electron affinity.[22−24] The utilization of terpyridine-based

Received: July 6, 2024
Revised: October 5, 2024
Accepted: October 8, 2024
Published: October 23, 2024

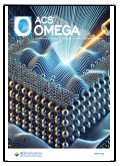

metal complexes has gained significant attention in contemporary research, particularly in supramolecular chemistry and applications in materials' sciences. They serve diverse roles including as active layers in resistive switching memory devices, fluorescent probes for pyrophosphate (PPi) detection, catalyst precursors for oxidation reactions, and constituents of photofunctional nanomaterials.[25−28] 4-Imidazole-2,6-di-(pyrazinyl)pyridine, with an analogue of terpyridine having two extra nitrogen atoms, is much less explored as a ligand. The presence of extra nitrogen atoms may play a role for both $\pi\cdots\pi$ and anion$\cdots\pi$ interactions simultaneously. Hence, we have replaced acetylpyridine by acetyl pyrazine to get analogue of terpyridine during the synthesis of ligand.

In pursuit of our interest in searching for the less explored terpyridine analogue complexes, we report herein the synthesis, crystallographic and spectral characterization, supramolecular behaviors, and photophysical properties of two new Ni(II) complexes. Complex **1** is formed by reacting with Ni-$(NO_3)_2.6H_2O$ and 4-imidazole-2,6-di(pyrazinyl)pyridine ($\mathbf{N_3L_1}$) in aqueous acetonitrile medium. Complex **2** is synthesized by treating $Ni(ClO_4)_2.6H_2O$ with $\mathbf{N_3L_1}$ in an aqueous acetonitrile medium. Generally chelating ligand with "N" donors are strong field in nature. The d^8 electronic configuration Ni(II) shows a stereochemical preference to square planar over octahedral with strong field ligand. To restrict Ni(II) from adopting a square planar arrangement, we strategically use tridentate NNN donor in 1:2 molar ratio to ensure octahedral geometry. There are a lot of driving factors accountable for tuning the origin of several supramolecular interactions like metal variation, ligand variation, same ligand with different substituents (in terms of electron donating or withdrawing substituents), counteranion variation, solvent variation, etc. Here in the present study purposefully we restrict us in analyzing the role of counteranions when other parameters become the same. Here, both the complexes adopt same di cationic moiety $[Ni(\mathbf{N_3L_1})_2]^{2+}$ (almost same crystallographic parameters) and only variation in their counteranions. Single crystal X-ray structural analysis shows that both the complexes (**1** and **2**) crystallize in a monoclinic system with the space group $C2/c$ and their unit cell comprises eight complex units. It is noted that the variation in the auxiliary anion exhibits structural distinctions in the present complexes substantially. Both complexes form a similar type of 2D supramolecular assembly through intermolecular $\pi\cdots\pi$ stacking interactions. Additionally, complex **1** forms a 1D supramolecular chain, whereas complex **2** develops a 2D supramolecular architecture facilitated by various anion$\cdots\pi$ interactions. Furthermore, each complex also assembles into different 1D supramolecular chains via multiple intermolecular hydrogen bonding interactions. The distinct anion$\cdots\pi$ interaction modes with different extents were analyzed by using DFT calculations, complemented by the quantum theory of atoms-in-molecules (QTAIM) and the NCI plot index as computational tools. We also explored the electrical properties of both complexes. Experimentally, we assessed the potential of these synthesized complexes for application in photosensitive electronic devices such as Schottky barrier diodes (SBDs). It was determined that complex **2**, containing perchlorate anions, exhibited superior performance. This behavior was elucidated by using DFT calculations to provide a theoretical foundation for the observed experimental results.

EXPERIMENTAL SECTION

Materials and Apparatus. All chemical reagents of analytical grade and solvents of spectroscopic grade were purchased from commercial suppliers and employed without further purification. Freshly prepared doubly distilled water was utilized throughout the synthetic process, and all reactions were conducted under aerobic conditions. Elemental analyses (carbon, hydrogen, and nitrogen) were conducted using a PerkinElmer 2400 Series-II CHN analyzer, USA. ^{1}H NMR and ^{13}C NMR spectra were acquired employing a Bruker spectrometer operating at 400 and 100 MHz respectively with DMSO-d_6 serving as the solvent and tetramethylsilane (TMS) as the internal standard. Fourier transform infrared (FTIR) spectra were captured using a PerkinElmer LX-1 FT-IR spectrophotometer over the range of 4000 to 400 cm^{-1}, utilizing a contemporary diamond attenuated total reflectance (ATR) accessory. Mass spectra (ESI-MS) were obtained utilizing a Water HRMS model XEVO-G2QTOF#YCA351 spectrometer. A semiconductor parameter analyzer (Keithley 4200S) coupled with source-measure units (SMUs) was used to conduct the electrical characterizations of the Schottky devices at room temperature (300 K) under dark conditions. The ground state absorption spectra from the respective complexes (spin-coated thin films on a glass substrate) were taken using a UV−Vis-NIR spectrophotometer (Avaspec-3648).

Synthesis of 4-Imidazole-2,6-di(pyrazinyl)pyridine [$\mathbf{N_3L_1}$]. Acetylpyrazine (0.281 g, 2.3 mmol) was added to the ethanolic solution (30 mL) of imidazole-2-carboxaldehyde (0.09 g, 1 mmol) under star condition. Two mL of 1 M aqueous solution of KOH followed by 6 mL of aqueous NH_3 (35%) solution were poured into the reaction mixture at room temperature (Scheme S1, Supporting Information). The reaction mixture was then refluxed for 3 h, cooled at room temperature. An off-white solid was formed which was collected by filtration and washed with cold water for several times and dried in air. The desired product was obtained with satisfactory yield and acceptable purity (Yield 0.214 g (62%). m.p.>275 °C, Scheme S1 (Supporting Information). Anal. Calculated for $C_{16}H_{11}N_7$, C 63.79, H 3.65, N 32.56%. Found: C 63.69, H 3.60, N 32.51%. ^{1}H NMR (400 MHz, DMSO−D_6): δ (ppm) = 13.34 (s, 1H, NH), 9.89 (s, 2H, pyrazine H), 9.02 (s, 2H, pyridine H), 8.81−8.84 (m, 4H, pyrazine H), 7.45 (s, 1H, imidazole H), 7.23 (s, 1H, imidazole H) (Figure S1, Supporting Information). ^{13}C NMR (100 MHz, DMSO−D_6): δ (ppm) = 154.78, 150.18, 146.01, 144.55, 143.49, 143.47, 140.72, 130.88, 120.36, 117.21 (Figure S2, Supporting Information). Main FT-IR absorptions (KBr, cm^{-1}): 3280(bs), 1610(vs), 1546(vs), 1519(s), 1461(s), 1368(s), 1319(s), 1113(s), 1018(vs), 850(vs), 719(s), 705(vs) (Figure S3, Supporting Information). ESI-MS: m/z 324.097, calcd. for $[C_{16}H_{11}N_7+Na]^+$ 324.11 (Figure S4, Supporting Information).

Synthesis of $[Ni(\mathbf{N_3L_1})_2](NO_3)_2$ (Complex 1). An aqueous solution (5 mL) of $Ni(NO_3)_2.6H_2O$ (0.293 g, 1.0 mmol) was added dropwise to a suspension (20 mL) of the ligand, $\mathbf{N_3L_1}$ (0.602 g, 2.0 mmol) in acetonitrile with constant stirring for 2 h (Scheme S2, Supporting Information)at 70 °C. An olive-green colored solution was obtained after 10 min of complete addition. The solution was then filtered, and the filtrate was kept undisturbed for crystallization. After 2 weeks, brown X-ray quality crystals of complex **1** was obtained from the mother liquor (yield: 41%). Anal. Calculated for $C_{32}H_{22}N_{16}NiO_6$: C,

https://doi.org/10.1021/acsomega.4c06270
ACS Omega 2024, 9, 44494−44506

48.89; H, 2.80; N, 28.52%. Found: C, 48.70; H, 2.76; N, 28.47%. Main FTIR absorptions (KBr, cm^{-1}): 3212(bs), 1621(vs), 1478(vs), 1455(vs), 1435(vs), 1316(s), 1160(vs), 1036(vs), 852(vs), 416(vs) (Figure S5, Supporting Information).

Synthesis of $[Ni(N_3L_1)_2](ClO_4)_2$ (Complex 2). An aqueous solution (5 mL) of $Ni(ClO_4)_2.6H_2O$ (0.365 g, 1.0 mmol) was added dropwise to an a suspension (20 mL) of the ligand, N_3L_1 (0.602 g, 2.0 mmol) in acetonitrile with constant stirring for 2 h (Scheme S2, Supporting Information) at 70 °C when an olive green colored solution was obtained after 10 min of complete addition. The solution was then filtered and the filtrate was kept undisturbed for crystallization. After 3 weeks, red colored X-ray quality crystals of complex **2** were obtained from the mother liquor (yield: 48%). Anal. Calculated for $C_{32}H_{22}Cl_2N_{14}NiO_8$: C, 44.63; H, 2.55; N, 22.78%. Found: C, 45.58; H, 2.51; N, 21.72%. Main FTIR absorptions (KBr, cm^{-1}): 3402(bs),1621(s), 1481(vs), 1459(vs), 1441(vs), 1408(vs), 1060(s), 619(s), 852(s), 420(s) (Figure S6, Supporting Information).

(Caution! Salts of perchlorate are potentially explosive. Only small amounts of materials should be prepared and handled with extreme care.)

Details of X-ray crystallographic analysis, theoretical methods, and device fabrication have been provided in the Supporting Information.

RESULTS AND DISCUSSION

Structural Description with Comparison for Complexes 1 and 2. The molecular structure of complex **1** and complex **2** with the selected atom numbering scheme is shown in Figure 1 and Figure 2 respectively. Structural analysis reveals

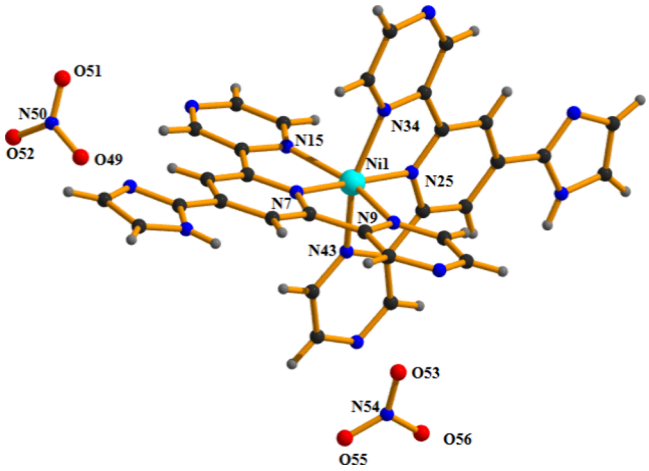

Figure 1. Molecular structure of complex **1**.

that both complexes crystallize in a monoclinic system with the space group *C*2/*c* and their unit cell comprises eight complex units (Table S1).

For both complexes, the selected bond lengths (Å) and bond angles (deg) are scheduled in Tables S2 and S3, respectively (Supporting Information). Both the complexes contain a general formula: $[Ni(N_3L_1)_2](X)_2$[X = NO_3^- for complex **1** and X = ClO_4^- for complex **2**] where N_3L_1 [4-imidazole-2,6-di(pyrazinyl)pyridine] acts as a tridentate chelating ligand. It is noteworthy to mention that the variation in counterions not only show architectural differences but also

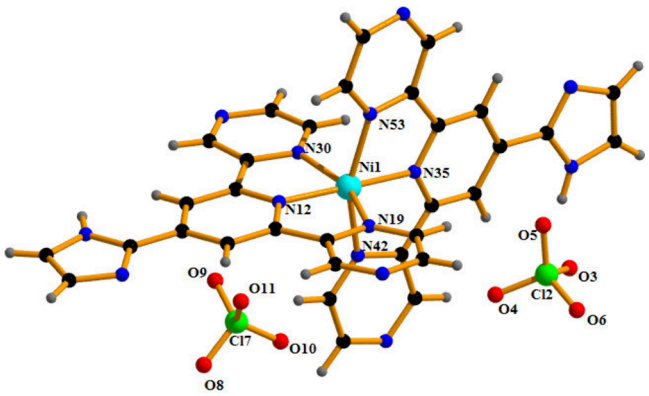

Figure 2. Molecular structure of complex **2**.

play a significant role in controlling the extent of supramolecular behaviors for the present complexes. The coordination mode around the metal center can be best described as the meridional geometry of distorted octahedron for both the complexes. For complex **1**, the two pyrazinyl nitrogen atoms (N15 and N9) and the two pyridyl nitrogen atoms (N7 and N25) of our title ligand (N_3L_1) generate the basal plane, while the axial positions are occupied by another two pyrazinyl nitrogen atoms (N34 and N43). The average Ni−N bond distance is 2.07 Å [Ni1−N7 = 1.998(3) Å, Ni1−N15 = 2.103(3) Å, Ni1−N25 = 1.990(3) Å and Ni1−N9 = 2.098(3) Å]. The axial nitrogen atoms are positioned somewhere at a longer distance [Ni1−N34 = 2.106(2) Å and Ni1−N43 = 2.110(4) Å] than the equatorial bond distance [$Ni1-N_{av}$ = 2.07 Å]. For complex **2**, the basal plane is formed by the two pyrazinyl nitrogen atoms (N19 and N30) and the two pyridyl nitrogen atoms (N35 and N12) of the title ligand (N_3L_1). The *trans* axial positions are occupied by two pyrazinyl nitrogen atoms (N42 and N53) of the title ligand (N_3L_1). In the basal plane, the Ni1−N bond lengths vary from 1.985(3) to 2.106(3) Å, whereas the axial Ni−N bond lengths [2.125(3) and 2.109(3) Å] are longer compared to the equatorial bond lengths likely to maintain the stereo relaxation and obtained stability by lowering the symmetry. Ni−N (nitrogen atoms come from pyridine and pyrazine moiety) bond distance ranges from 1.990 and 2.110 Å. As per data available from the crystallographic database the average Ni−N(pyridine) and Ni−N(pyrazine) bond distances are 2.06 and 2.15 Å. From the data it is evident that pyridine (the presence of one nitrogen atom) can form a comparatively stronger bond compared to pyrazine (the presence of two nitrogen atoms). Hence Ni−N(pyridine) bond distances are shorter than those of Ni−N(pyrazine). The average metal centric bond angles ∠N−Ni−N are 105.29° for complex **1** and 105.5° for complex **2**. In complex **1**, the Ni(II) ion is deviated by a distance of 0.023 Å toward the axial nitrogen atom (N34) from the basal plane (N15N7N9N25) whereas in complex **2**, the same is 0.017 Å toward the axial N53 atom from the basal plane (N35N30N12N19). The electrical charge of the Ni(II) cationic moiety is taken care by two noncoordinated nitrate (NO_3^-) and perchlorate (ClO_4^-) ions for complex **1** and **2** respectively. Here in the present work, the title ligand (N_3L_1) utilizes two pyrazine atoms and one pyrazine nitrogen atom in the coordination game. Through this coordination (to metal Ni^{II}), the aromatic rings become electron deficient and are suitable for anion···π interaction. In case of peripheral imidazole ring, the ring N−H bond participates in classical

https://doi.org/10.1021/acsomega.4c06270
ACS Omega 2024, 9, 44494−44506

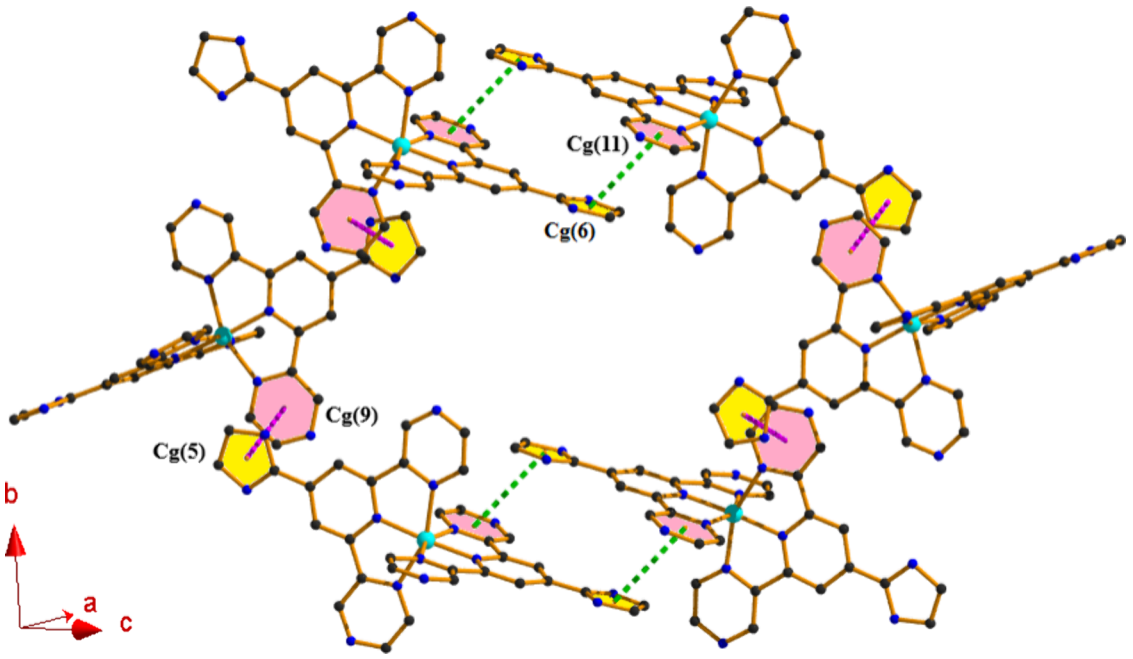

Figure 3. Perspective view of 2-D architecture incorporating $\pi\cdots\pi$ interactions in complex **1** (hydrogen atoms have been omitted for clarity).

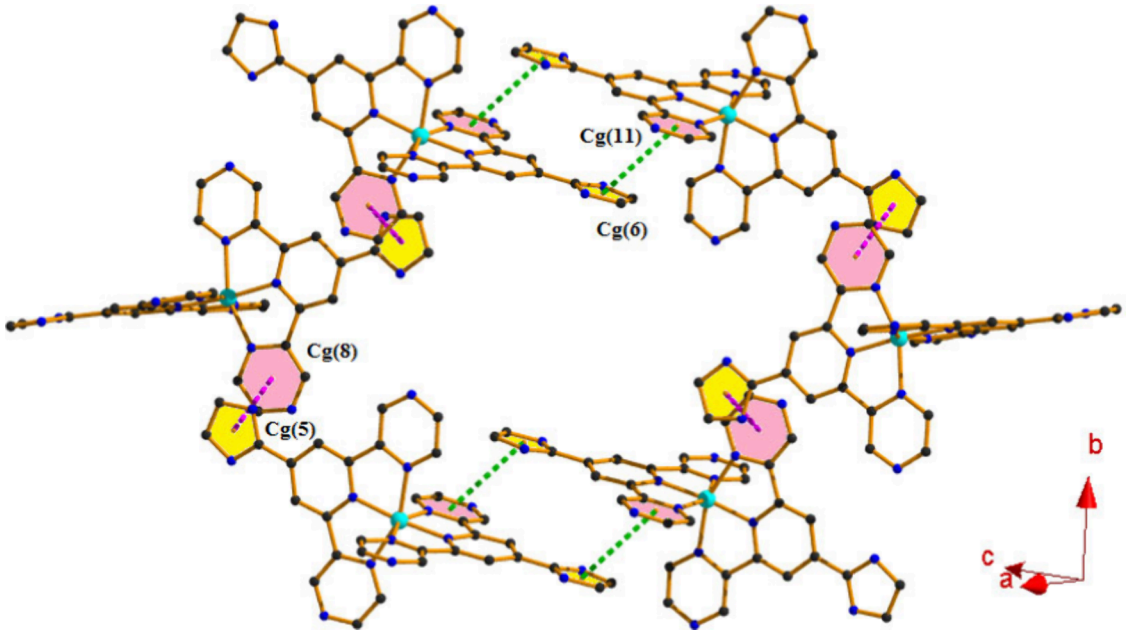

Figure 4. Perspective view of 2-D architecture incorporating $\pi\cdots\pi$ interactions in complex **2** (hydrogen atoms have been omitted for the sake of clarity).

N−H···O hydrogen bonding interaction and make it to some extent eligible to ensure anion···π interaction. From a structural point of view, we may conclude that central pyridine and two substituted pyrazine rings became more electropositive character (as directly involved in metal coordination) compared to the peripheral imidazole ring (involved in weak H-bonding interaction compared to imidazole rings).

The solid-state structures of both the complexes are stabilized through the combination of $\pi\cdots\pi$, anion···π, and various types of hydrogen bonding interactions (Tables S4, S5 and S6). The complex units of **1** form a dimeric assembly through the self-complementary $\pi\cdots\pi$ interactions (Table S5, Supporting Information) between Cg(6) of one unit and Cg(11) of the other unit at $(1-x, 1-y, 1-z)$ having a separation distance of 3.735(2) Å. The dimeric units are further connected at $(1/2-x, -1/2+y, 1/2-z)$ through another self-complementary $\pi\cdots\pi$ interactions between Cg(5) and Cg(9) of two different complex units with the separation distance of 3.578(2) Å. These interactions are repeated in such a fashion so that they form a 2D cage like supramolecular architecture in the *bc* plane which is depicted in Figure 3.

A very similar type of supramolecular architecture (as that of complex **1**, Figure 3) is formed for complex **2** as shown in Figure 4. Here, the complex units of **2** form a dimeric assembly through the self-complementary $\pi\cdots\pi$ interactions (Table S5, Supporting Information) between Cg(6) of one unit and

https://doi.org/10.1021/acsomega.4c06270
ACS Omega 2024, 9, 44494−44506

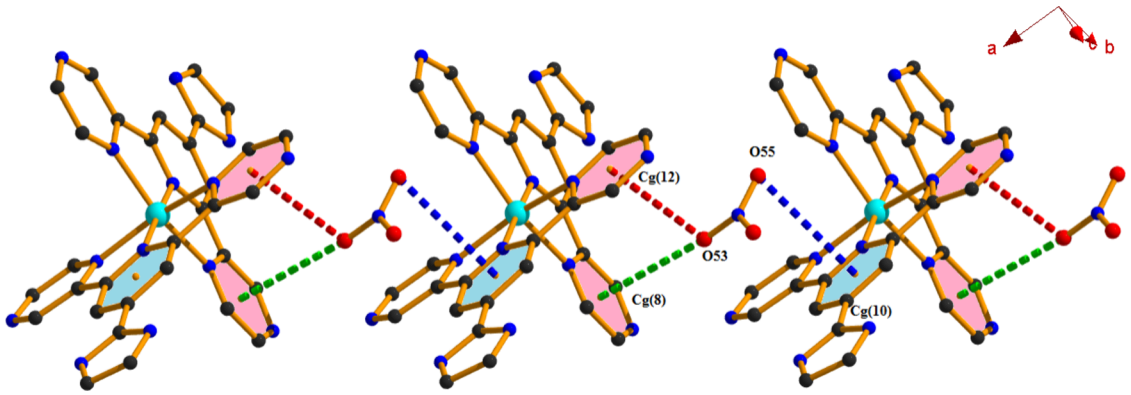

Figure 5. 1-D supramolecular chain generated through various anion···π interactions in complex **1** (hydrogen atoms have been omitted for the sake of clarity).

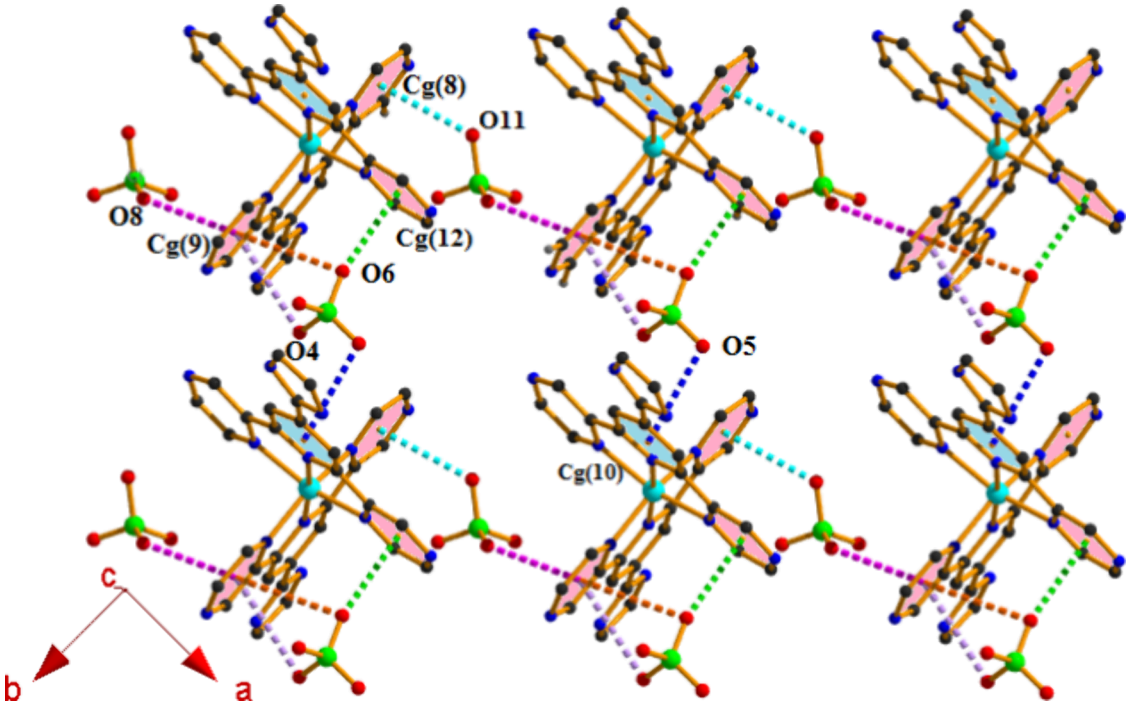

Figure 6. 2-D layer generated through various anion···π interactions in complex **2** (hydrogen atoms have been omitted for the sake of clarity).

Cg(11) of the other unit at $(1-x, 1-y, 1-z)$. The dimeric units are further connected through another self-complementary $\pi\cdots\pi$ interactions between Cg(5) of one unit with Cg(8) of the other unit at $(1/2-x, -1/2+y, 1/2-z)$ and form a 2D cage like supramolecular architecture in *ab* plane which is depicted in Figure 4. The interplanar separation distances between consecutive Cg(6)−Cg(11) and Cg(5)−Cg(8) centroids are 3.831(2) and 3.667(2) Å respectively.

Furthermore, the monomeric units of complex **2** are connected through a self-complementary $\pi\cdots\pi$ interaction between Cg(5) and Cg(7) of two units at $(-x, y, 1/2-z)$ to form a dimeric assembly which is further linked through another self-complementary $\pi\cdots\pi$ interaction between Cg(6) and Cg(12) of two different units at $(1-x, 1-y, 1-z)$ to form a 1D supramolecular chain (Figure S7). The ring centroid separation between Cg(5) and Cg(7) is 3.716(2)Å and the ring centroid separation between Cg(6) and Cg(12) is 3.553(2) Å (Table S5, Supporting Information).

Besides $\pi\cdots\pi$ interactions, anion···π interactions play a crucial role in the crystal packing for both complexes in the solid state. In complex **1**, the one-dimensional (1-D) supramolecular chain is generated through various anion···π interactions (Figure 5). Here the noncoordinating nitrate (NO_3^-) ion interacts simultaneously with Cg(8) at (x, y, z) and Cg(12) at (x, y, z) of the complex unit and Cg(10) of another unit at $(-1/2+x, 1/2+y, z)$ having an average anion···π separation distance of 3.666 Å.

A 2-D layer is shaped in complex **2** using various anion···π interactions (Figure 6) incorporating noncoordinating perchlorate anions. Here, both perchlorate ions act as connectors among the monomeric units of complex **2**. As depicted in Figure 6, oxygen atoms (O11 and O8) of one perchlorate anion interact simultaneously with Cg(8) at $(-x, y, 1/2-z)$ and with Cg(9) at $(1/2-x, -1/2+y, 1/2-z)$ having angles 124.3(4)° and 131.7(3)°, respectively, to produce a 1D polymeric chain. Then these polymeric chains placed in parallel are further linked through the other perchlorate anion,

https://doi.org/10.1021/acsomega.4c06270
ACS Omega 2024, 9, 44494−44506

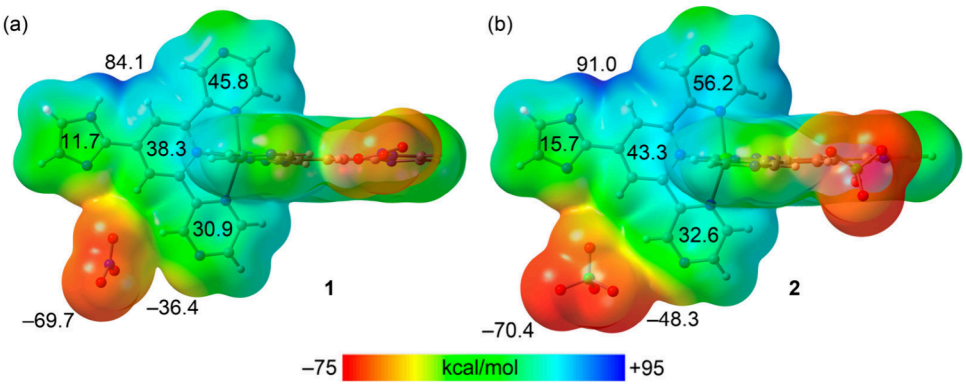

Figure 7. MEP surfaces (isosurface 0.001 au) of complexes **1** (a) and **2** (b) at the PBE0-D3/def2-TZVP level of theory. The values at selected points of the surface are given in kcal mol^{-1}.

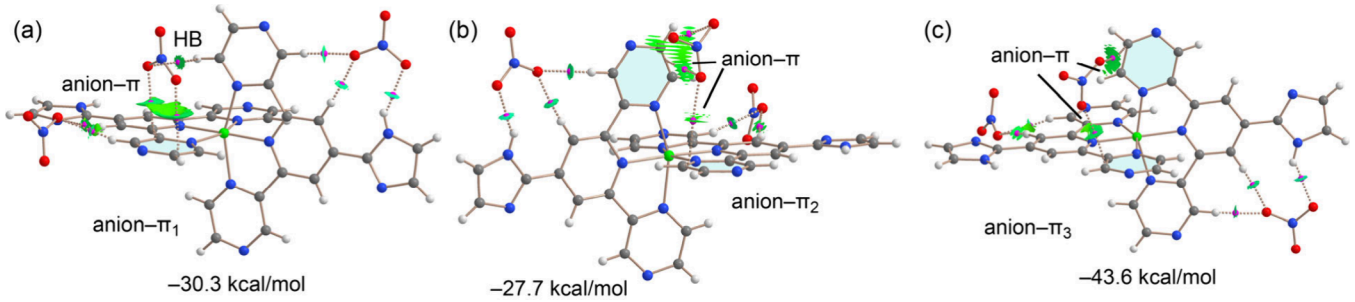

Figure 8. Distribution of BCP (magenta spheres) and bond paths dashed lines anion···π_1 (a), anion···π_2 (b) and anion···π_3 (c) binding modes at the PBE0-D3/def2-TZVP level of theory for complex **1**. The overlapped NCI plot has been constructed using the 0.5 au RGD isosurface and the sign $(\lambda_2)\rho$ have been mapped using the ρ = 0.04 au cutoff. For clarity, only the intermolecular interactions are represented.

which are involved in mutual interactions between O6 and Cg(9) at (1/2+*x*, −1/2+*y*, *z*), O6 and Cg(12) at (1/2+*x*, −1/2+*y*, *z*), O4 and Cg(9) at (1/2+*x*, −1/2+*y*, *z*) and O5 and Cg(10) at (*x*, *y*, *z*) having angles 95.5(2)°, 158.4(3)°, 95.3(3)° and 107.6(3)° respectively. These interactions are responsible to enhance the dimensionality to 2D. The average O···Cg (anion···π) distance is 3.277 Å (which is much lower than that of complex **1**); representing comparatively stronger anion···π interactions.

It is noteworthy to mention that in complex **1**, only one noncoordinating NO_3^- ion is involved in the said intermolecular anion···π interactions (Figure 5) leaving the other NO_3^- ion (that is not involved in extending the dimensionality) with the complex unit, whereas in complex **2**, both the ClO_4^- ions are involved in the intermolecular (involved in extending the dimensionality) anion···π interactions (as depicted in Figure 6).

The complex units are further interlinked through various hydrogen bonding interactions [C22−H22···O53 (163°), C16−H16···O55 (155°), C29−H29···O56 (173°), C47−H47···O56 (172°), and C41−H41···O55 (143°)] to form a zigzag polymeric chain along the [001] direction (Figure S8) in complex **1**. In addition, a 1D chain is generated through three different C−H···O hydrogen bonding [C5−H5···O49 (163°), C40−H40···O52(131°), and C19−H19···O49 (163°)] interactions as shown in Figure S9 for complex **1**.

In complex **2**, two different 1D supramolecular chains are formed by using only C−H···O hydrogen bonding interactions (see Figures S10 and S11). In Figure S10, perchlorate ion interacts with the complex units involving C27−H27···O6(170°) and C57−H57···O5 (174°) hydrogen bonding interactions, whereas in Figure S11, perchlorate ion binds with the complex units through C23−H23···O10(139°), C49−H49···O11(138°), C50−H50···O8(132°), and C14−H14···O9 (161°) hydrogen bonding interactions. The other geometrical parameters such as H···A (Å), D···A (Å), symmetry, etc. for the said hydrogen bonding interactions are given in the Supporting Information part (See Table S4).

From the structural elucidation, we may conclude that even after variation in anionic part (perchlorate and nitrate) the basic stereochemical properties become almost the same and that is reflected in their virtually comparable crystal packing parameters. The basic difference in the two counteranions are as follows: nitrate (NO_3^-) is planner and perchlorate ion (ClO_4^-) is tetrahedral. As noncovalent interactions are directional in nature, 3D alignment of perchlorate ion is responsible to enhance the extent of anion···π interactions in **2** (both perchlorates are participating in stronger intermolecular anion···π interactions with high extent) over 2D nitrate anions in **1**.

DFT Calculations. The theoretical study delves into the anion···π binding modes observed in the solid state of complexes **1** and **2**, where the dication $[Ni(\mathbf{N_3L_1})_2]^{2+}$ interacts with nitrate and perchlorate counterions through a synergy of hydrogen bonds and anion···π interactions. This section employs DFT calculations, molecular electrostatic potential (MEP) analysis, and a combination of QTAIM and NCI Plot computational tools to further dissect these interactions.

Initially, MEP surfaces of the $[Ni(\mathbf{N_3L_1})_2](NO_3)_2$ (**1**) and $[Ni(\mathbf{N_3L_1})_2](ClO_4)_2$ (**2**) complexes were calculated to identify the most electrophilic regions in a neutral system, highlighting areas conducive to electrophilic attack. The analysis facilitated a comparison of the ability of different rings within the 4-imidazole-2,6-di(pyrazinyl)pyridine ligand ($\mathbf{N_3L_1}$) to form

https://doi.org/10.1021/acsomega.4c06270
ACS Omega 2024, 9, 44494−44506

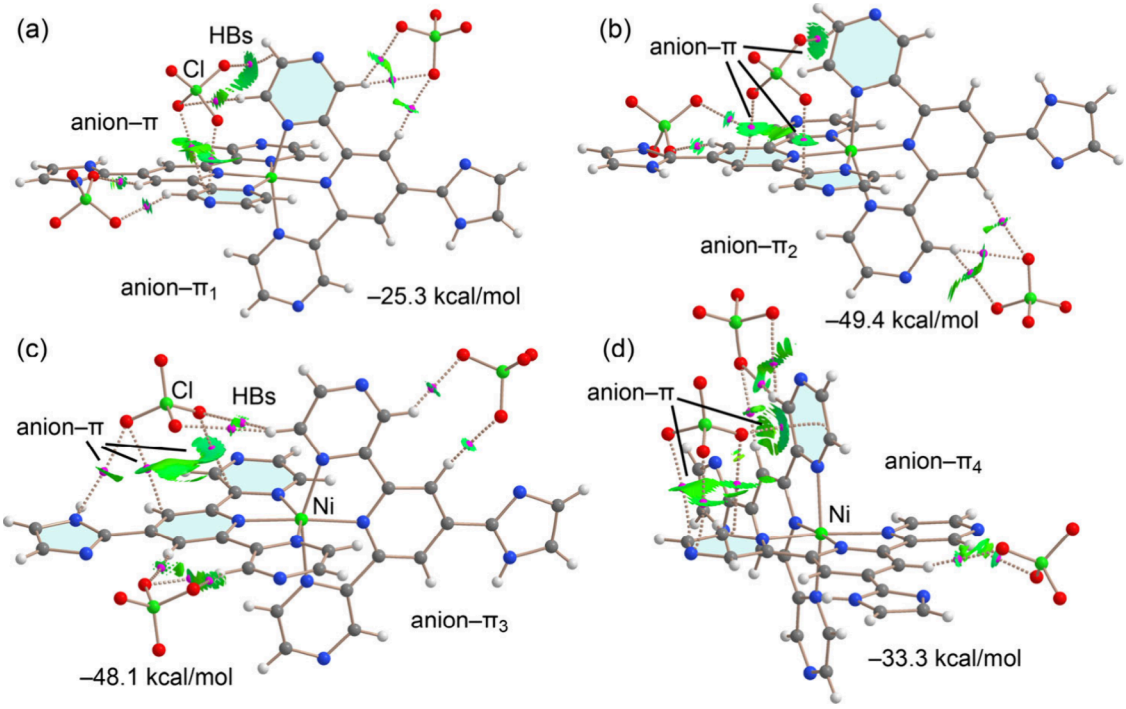

Figure 9. Distribution of BCP (magenta spheres) and bond paths dashed lines anion···π_1 (a), anion···π_2 (b), anion···π_3 (c) and anion···π_4 (d) binding modes at the PBE0-D3/def2-TZVP level of theory for complex **2**. The overlapped NCI plot has been constructed using the 0.5 au RGD isosurface and the sign $(\lambda_2)\rho$ has been mapped using the ρ = 0.04 au cutoff. For the sake of clarity, only the intermolecular interactions are represented.

anion···π interactions with the counterions to different extent. Displayed in Figure 7, the MEP maxima at the NH groups of the imidazole rings are 84.1 and 91.0 kcal/mol for complexes **1** and **2**, respectively. Correspondingly, the MEP minima at the nitrate and perchlorate counterions are 69.7 and −70.4 kcal/mol. Additionally, high and positive MEP values were observed over the centers of the three aromatic rings coordinated to the Ni(II) ion, with values spanning from 30.9 to 56.2 kcal/mol across the pyridine and pyrazine rings in the two complexes, indicating significant variations linked to their proximity to the H-bonded anions. Notably, the MEP over the five-membered imidazole ring is substantially lower, consistent with the absence of anion···π interactions involving this ring in the description of the solid-state structures of complexes **1** and **2**.

We examined the interaction energies associated with the anion···π interactions in both complexes, which are discernible in three distinct modes in the solid state of complex **1**, as depicted in Figure 8. These interactions are labeled as anion···π_1, anion···π_2, and anion···π_3. In anion···π_1 (Figure 8a), the nitrate anion is positioned approximately over the center of a pyrazine ring. QTAIM analysis indicates that two O atoms of the nitrate are linked to the aromatic ring by two bond critical points (BCPs) and bond paths, with an additional RDG isosurface encompassing the region between the anion and most of the aromatic ring. Additionally, another BCP links an O atom to an aromatic hydroxyl atom of the pyrazine from another ligand.

In the anion···π_2 configuration, the anion interacts with two different pyrazine rings: one parallel with two BCPs and bond paths connecting the anion and pyrazine, and another perpendicular, with one O atom linked to the pyrazine (as shown in Figure 8b). The anion···π_3 (as shown in Figure 8c) mode involves interactions with two pyrazine rings, both in a perpendicular arrangement, where two O atoms of the nitrate anion are connected to two different pyrazine rings through their respective BCPs, bond paths, and green RDG isosurfaces.

The binding energies, depicted in Figure 8, were calculated for dimers. In these calculations, the $[Ni(N_3L_1)_2](NO_3)_2$ complex is considered as a monomer that interacts with an anion···π bonded nitrate. The interaction energies show that the anion···π_3 mode is the most favored, with a significant energy of −43.6 kcal/mol, while the other two modes present similar energies of −30.3 and −27.7 kcal/mol for anion···π_1 and anion···π_2, respectively. These substantial interaction energies corroborate the strong electrophilicity of the complex, as indicated by the MEP surface analysis.

Four distinct types of anion···π interactions are observed in the solid state of complex **2**, as shown in Figure 9, labeled as anion···π_1, anion···π_2, anion···π_3, and anion···π_4. In anion···π_1 (Figure 9a), the perchlorate anion is positioned centrally above one pyrazine ring, akin to the anion···π_1 mode observed in complex **1**. QTAIM analysis reveals that two O atoms of the perchlorate are linked to the pyrazine ring via two BCPs and bond paths. Additionally, a substantial RDG isosurface covers much of the region between the anion and the aromatic ring, delineating the anion···π interaction. The QTAIM analysis also identifies two additional BCPs connecting two O atoms to two aromatic H atoms on the pyrazine ring from another ligand, further stabilizing this arrangement.

In the anion···π_2 mode (Figure 9b), the perchlorate anion interacts with two pyrazine rings and one pyridine ring, forming three BCPs and bond paths that link three O atoms to the aromatic rings. The anion···π_3 mode (Figure 9c) involves interactions between the anion and three aromatic rings, including the imidazole, with three BCPs and bond paths connecting only two O atoms of the perchlorate to the rings.

https://doi.org/10.1021/acsomega.4c06270
ACS Omega 2024, 9, 44494−44506

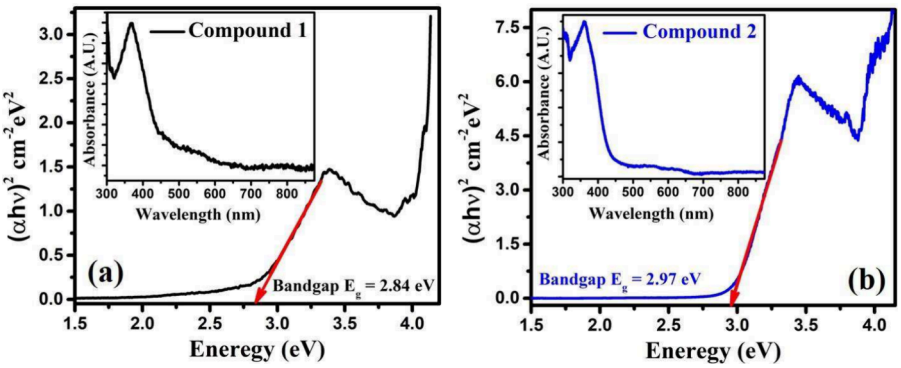

Figure 10. Tauc plots $[(\alpha h\nu)^2$vs $h\nu]$ to estimate the HOMO − LUMO of (a) complex **1**, and (b) complex **2**. Inset shows corresponding UV−visible absorption spectra.

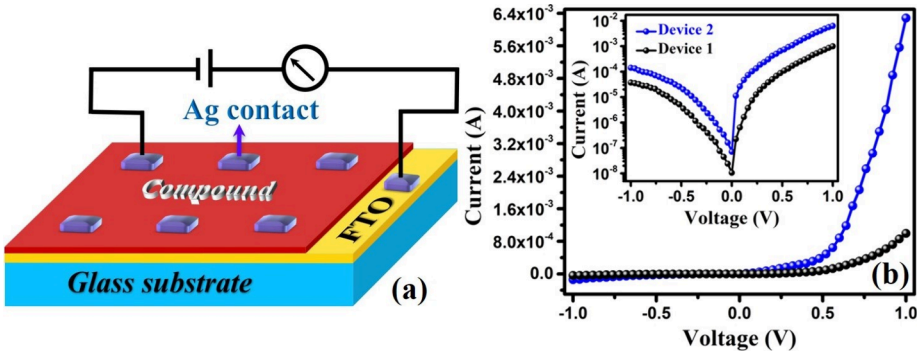

Figure 11. (a) Schematic illustration of the fabricated Schottky device (diode) structure. (b) I−V characteristic curves from Schottky devices **1** and **2**, under dark conditions. The Inset figure represents the current in logarithmic scale as a function of voltage.

The QTAIM/NCI Plot analysis additionally highlights the formation of two supplementary H-bonds.

Lastly, the anion$\cdots\pi_4$ mode (Figure 9d) demonstrates the perchlorate anion engaging with one pyrazine ring of one ligand via three BCPs and bond paths while simultaneously linking to another pyrazine of a different ligand through a single BCP and bond path. Both are also characterized by green RDG isosurfaces.

The binding energies reveal that the anion$-\pi_2$ and anion$-\pi_3$ modes are more energetically favorable (−49.4 and −48.1 kcal/mol, respectively) compared to the other modes (−25.3 kcal/mol for anion$-\pi_1$ and −33.3 kcal/mol for anion$\cdots\pi_4$), mirroring the high stability observed in the anion$\cdots\pi_3$ configuration of complex **1**.

Optical Study. To determine the optical bandgap of the complexes, UV−vis-NIR absorption spectra were recorded. Figure 10(a) and 10(b) show UV−vis-NIR absorption spectra obtained from the complexes **1** and **2** spin-coated thin films on glass substrates, respectively. Quite similar and strong absorption features in the visible spectral range have been observed from both the complexes. We have evaluated the optical bandgap of the complexes utilizing the following Tauc relation (1)

$$(\alpha h\nu) = A(h\nu - E_g)^n \quad (1)$$

Where α stands for absorption coefficient, $h\nu$ is the photon energy, A is a proportionality constant (independent of wavelength), E_g represents the energy gap between the HOMO − LUMO levels of the complex, and coefficient "n" takes the value 1/2 for this case. Now it simply from the above eq 1, that the spectral dependence of the absorption coefficient must linearize in Tauc's plot $[(\alpha h\nu)^2 vs\ h\nu]$ and the x-axis intercept position for $\alpha = 0$ will give the HOMO − LUMO energy gap of the material. The HOMO − LUMO gaps (E_g) were determined to be 2.84 and 2.97 eV, respectively, for complexes **1** and **2** (Figures 10a and 10b). These findings indicate that we may suitably explore UV photodetection applications with these complexes, provided they exhibit good transport properties (such as conductivity, mobility, etc.).

Electrical Study. Current (I) vs Voltage (V) characteristics of both Devices 1 and 2, were performed at 298 K in the applied voltage range between −1 and +1 V under dark conditions. Figure 11(a) shows the schematic representation of the sandwiched Schottky device structure. Figure 11(b) shows the $I-V$ characteristic curves offered by both Devices under dark conditions, demonstrating the typical nonlinear and rectifying nature of Schottky barrier diodes (SBD). The current rectification ratio, which is defined as the current at the forward voltage to that of the reverse voltage, is found to be higher (45) for Device 2 in comparison to Device 1 (27) at ±1 V. This implies that, when it comes to rectifier devices, Device 2 (complex **2**) will function better than Device 1 (complex **1**). Conductivity measurement of the devices implies that in terms of electron transportation capability, Device 2 is superior to that of Device 1. By analyzing the linear regions of the $I-V$ characteristic curves, conductivity (σ) for Device 1 was found to be 5.52×10^{-7} S cm^{-1} and 1.66×10^{-6} S cm^{-1} for Device 2 at 298 K. Although these conductivity values appear a bit low but there are several reports of similar or even lower conductivities in Ni(II), Co(II) and Cu(II) complexes (Table S8). Even though Device 2 (i.e., complex **2**) delivered a better charge transport property compared to Device 1 (i.e.,

https://doi.org/10.1021/acsomega.4c06270
ACS Omega 2024, 9, 44494−44506

complex **1**), still it does not meet the minimum requirement in terms of conductivity for efficient optoelectronic applications.

We must closely examine these rectified $I-V$ curves in order to comprehend the main charge transfer mechanisms. These nonlinear as well as rectifying $I-V$ attributes of the devices can be described using a Richardson−Schottky equation considering thermionic emission and diffusion of carriers over barriers.[29,30] As these complexes exhibit a wide band gap, hence we can apply thermionic emission theory to study the present cases.[31] According to this theory, the dark $I-V$ characteristics of both the Schottky devices can be expressed as[30,31]

$$I = I_s\left[\exp\left(\frac{qV}{\eta k_B T}\right) - 1\right] \tag{2}$$

where I and I_s are the forward current and reverse saturation current, V is the applied voltage, η is the ideality factor of the Schottky diode, q is the electronic charge, k_B is the Boltzmann constant and T is the absolute temperature. On the other hand, reverse saturation current (I_s) can be expressed as[29−31]

$$I_s = AA^*T^2\exp\left(\frac{-q\phi_B}{k_B T}\right) \tag{3}$$

where A defines active device area ($= 2.25 \times 10^{-2}$ cm^2), A^* ($=$ 132A K^{-2} cm^{-2}) is the Richardson constant, ϕ_B is the Schottky barrier height, k_B is the Boltzmann constant and T is the absolute temperature. Considering the diode series resistance R_s, forward $I-V$ characteristics for $V > \frac{3k_BT}{q}$ can be represented by the following equation,[29,32]

$$I = I_s\left[\exp\left(\frac{q(V - IR_s)}{\eta k_B T}\right)\right] \tag{4}$$

Here the term IR_S signifies the voltage drop across the series resistance R_S. Utilizing the eqs 3 and 4, Cheung et al. have developed two linear eqs eqs 5 and 6,[32] which can be employed to determine the ideality factor (η), Schottky barrier height (ϕ_B), and series resistance (R_s) of complex **1** and complex **2** based Schottky barrier devices.

$$G(I) = \frac{dV}{d(\ln I)} = \frac{\eta k_B T}{q} + IR_s \tag{5}$$

$$H(I) = IR_s + \eta\phi_B \tag{6}$$

where,

$$H(I) = V - \left(\frac{\eta k_B T}{q}\right)\ln\left(\frac{I}{AA^*T^2}\right)$$

Now following eq 5, from G(I) vs I graph we can calculate series resistance (R_S) from the slope and ideality factor (η) from the y-axis intercept, whereas from $H(I)$ vs I graph we can determine the value of Schottky barrier height (ϕ_B) from the y-axis intercept. $G(I)$ vs I and $H(I)$ vs I graphs, for the Device 1 have been shown in Figure S12(a) and those for the Device 2 have been displayed in Figure S12(b). The evaluated ideality factor (η) for Device 1 is 1.50, whereas for Device 2 it is 1.34. Deviation of η values from the ideal case ($\eta = 1$) implies that there is a formation of inappropriate metal−semiconductor junctions, led by the defect/trap states at the interface. It is known that the structural disorder of a complex affects the thin film quality and creates more clutter structures on the surface, which results in the creation of more defect states at the metal−semiconductor interface. As a result, that η value largely deviates from ideal value 1. Nonideality of the Schottky diode can also be attributed to surface contamination, barrier tunnelling, etc.[33,34]

The series resistance (R_s) which limits the flow of charge through the Device, is evaluated to be 3.41 k-ohm for Device 1, whereas that for Device 2 is found to be 1.1 k-ohm. Almost three times lower resistivity offered by the Device 2 compared to Device 1, clearly tells that there are comparatively less inhomogeneities in the metal−semiconductor junction of Device 2, which results in better carrier transportation.[35,36] These findings are consistent with earlier conductivity (σ) studies, where complex **2** delivered nearly three times better conductivity than complex **1**. Furthermore, it is discovered that the barrier height (ϕ_B) for Device 1 is found to be 0.52 eV whereas that for Device 2 is 0.46 eV. Device **2** therefore provides a lower Schottky barrier height than Device 1, as would be predicted. All the device parameters were evaluated from the electrical measurements carried out in dark conditions and have been listed in Table S7 (Supporting Information).

To induce conductivity, a number of efforts have been explored via through-bond, extended conjugation, and through-space involving weak interaction strategies.[37,38] In this work, charge transportation occurs through the combination of these three strategies. The extended conjugation in the ligand moiety and metal-induced charge transfer along with other weak interactions explain the higher conductivity in the title complexes. According to their band gap (2.84 for complex **1** and 2.97 for complex **2**), complex **1** should be more conducting in nature than that of complex **2**. But the interesting thing is that complex **2** exhibits comparatively higher conductivity than that of complex **1**. Here, such striking differences in device properties between the complexes can majorly be attributed to two factors: (i) the better partial electron transfer from ClO_4^- to the ligand moiety and vice versa through 2D supramolecular architecture in complex **2**, whereas in complex **1**, the electron transfer occurs from NO_3^- to the ligand moiety through 1D supramolecular chain and (ii) the greater number of $\pi\cdots\pi$ and anion$\cdots\pi$ interactions in complex **2** helps in the better electron transfer among ligand moieties than that in complex **1**.

Beside structural elucidation, the electronic properties of the complexes were investigated through their electrical conductivity. In both mentioned complexes, electron charge transportation may occur through extended conjugation provided by heterocyclic ligand moiety and charge transfer through intervening metal ions incorporating several ionic and noncovalent interactions.[38] From structural analysis, it is evident that the two complexes differ only by their noncoordinating counteranionic part. From the FMO approach, the energy difference between HOMO and LUMO may vary with electronic effect associated with complex systems. Therefore, a change in electron orbital composition of Ni(II) complexes, i.e., the energy levels of HOMO or LUMO of Ni(II), is significantly affected by both electron-donating or electron-withdrawing environment. The energy level of HOMO/LUMO were higher with electron withdrawing groups and lower with electron donating groups.[39] Both nitrate NO_3^- and perchlorate ClO_4^- are considered to be noncompressible, non- polarizable hard anions. Perchlorate

https://doi.org/10.1021/acsomega.4c06270
ACS Omega 2024, 9, 44494−44506

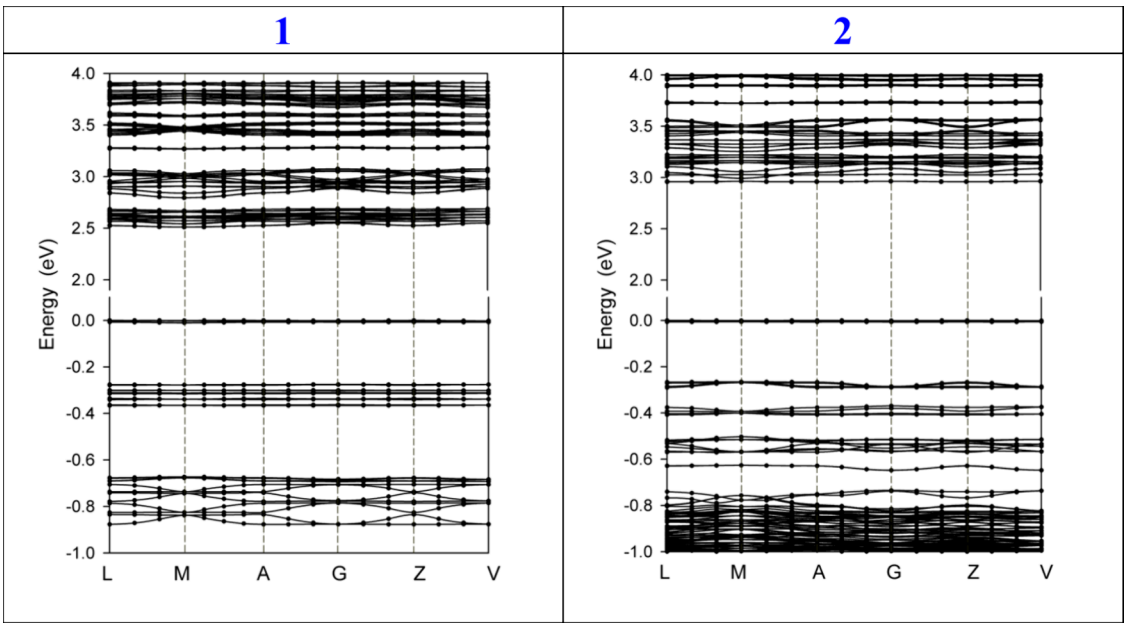

Figure 12. Electronic band structure of complex **1** and **2** crystals. Points of high symmetry in the first Brillouin zone are labeled as follows: L = (−0.5, 0, 0.5), M = (−0.5, 0.5, 0.5), A = (−0.5, 0, 0), G = (0, 0, 0), Z = (0, −0.5, 0.5) and V = (0, 0, 0.5).

ClO_4^- (Central "Cl" is in "+7" oxidation state) is more electron withdrawing than that of NO_3^- (Central "N" is in "+5" oxidation state), and henceforth ClO_4^- may be considered as more electronegative (that is, potent electron withdrawing) compared to nitrate (NO_3^-).

So the more electron-withdrawing perchlorate complex executes a higher HOMO−LUMO gap, which in turn results in a comparatively higher band gap. It is our general expectation that a higher band gap reduces electrical conductivity. For better electrical conductivity, a lower band gap is not the only decisive factor, but the ease of transportation may be enhanced through several intermolecular interactions (both covalent and noncovalent). From a structural aspect, it is already identified that in complex **2**, stronger anion···π interactions (Figure 6) due to 3D orientation of perchlorate ion, provides more scope for electron hopping through the anion···π cluster (more anion···π interaction in complex **2** compared to complex **1**) that in turn may result in higher conductivity of complex **2**. A few representative conductivity values of Ni(II), Co(II) and Cu(II) complexes are tabulated in Table S8.

Theoretical DFT Study of Electrical Properties. The crystal structures of 1 and 2 were modeled using DFT, with the experimental crystal lattices as the starting point for optimizing atomic positions. To evaluate the alignment between experimental data and theoretical predictions, we applied a standard band theory methodology. However, it is noteworthy that DFT commonly exhibits a tendency to underestimate semiconductor band gap values.[40] Hence, in order to address this, we systematically incorporated a 1.2 eV scissor operator across all of the analyzed crystals in this study. This adjustment allowed for a more accurate portrayal of the electronic structure and facilitated a more meaningful comparison between the theoretical simulations and experimental observations.

Based on the band diagram (Figure 12) and the partial density of states diagram (PDOS) (Figure 13), it is evident that the crystal demonstrates semiconductor characteristics. The band diagram in Figure 12 highlights the differences among the crystals investigated. In the conduction band region (0 to 4 eV), complex 1 exhibits up to five sets of bands with low dispersion within the range of 2.5 to 4 eV. In contrast, complex 2 only displays three sets within the range of 3 to 4 eV. However, upon examining the valence band region of both crystals (0.0 to −1.0 eV), subtle changes corresponding to the substitution of anions are discernible, resulting in differences in electronic characteristics. In the valence band region, both crystals feature a well-defined set of bands cantered around 0 eV with minimal dispersion. However, significant differences become apparent beyond this point. While complex 1 exhibits two additional band regions between −0.2 eV and −0.4 eV and between −0.65 eV and −0.90 eV within the same energy range, complex 2 displays multiple identifiable regions between −0.2 eV and −1.0 eV. As depicted in Figure 12, the localized regions in complex 1 can be attributed to the NO_3^- anions, which contribute alongside Nickel to the outermost valence bands. Conversely, this behavior is not observed when ClO_4^- anions are present in the structure, with the outer valence levels dominated by the p-orbitals of the N_3L_1 complex along with the d-orbitals of nickel.

Theoretically, it is possible to determine the frequency dependence of an incident photon in a material by calculating its dielectric function $\varepsilon(\omega)$ and optical conductivity ($\sigma(\omega)$). As shown in Figure S13, both Ni compounds exhibit similar diagrams concerning the intensity of their maxima between 0 and 6 eV, with different behavior beyond 6 eV. Typically, the photoconductivity, and consequently the electrical conductivity of materials, increases due to photon absorption. However, in this case, the experimental behavior does not follow this pattern.

As the concerned two complexes are ionic materials, the total conductivity in the presence of an electric field will be the sum of the electronic part and the ionic part:

$$\sigma = \sigma_e + \sigma_i \tag{7}$$

https://doi.org/10.1021/acsomega.4c06270
ACS Omega 2024, 9, 44494−44506

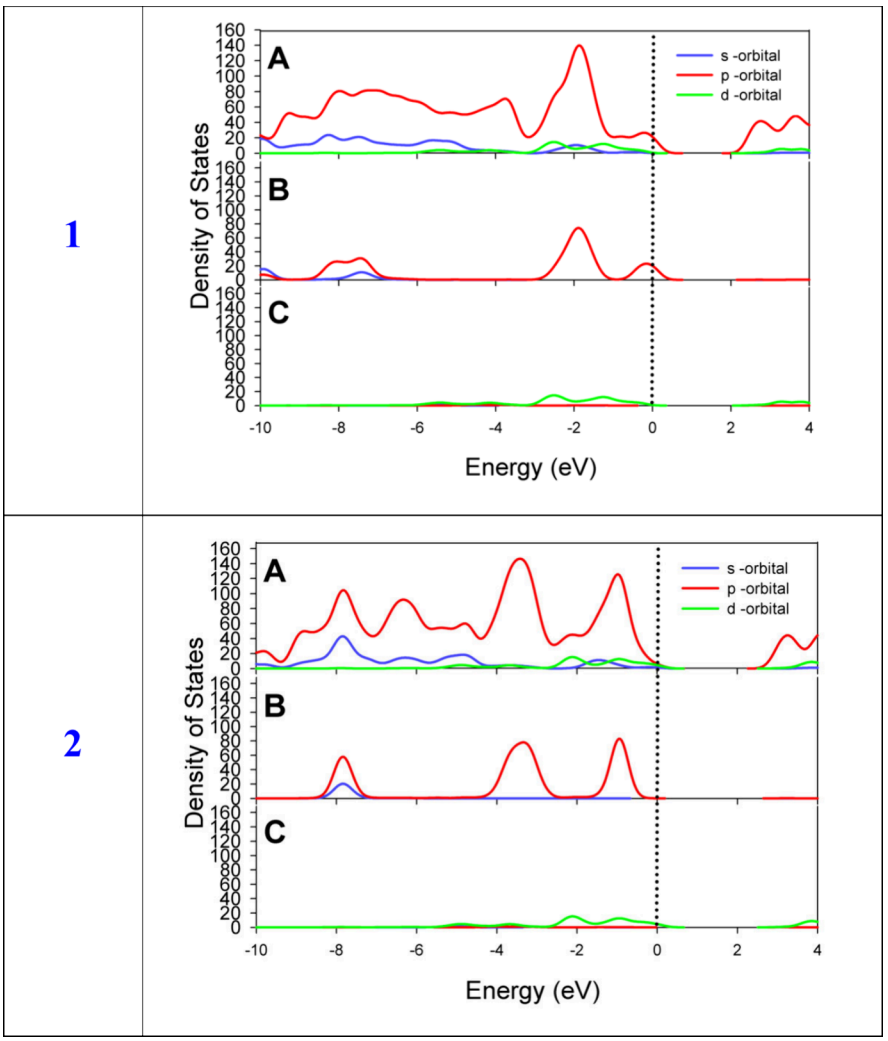

Figure 13. Calculated partial density of states for 1 and 2 crystal cells. Panels depict: 1) A.) Entire system, B.) NO_3^- anion, and C.) Ni metal; 2) A.) Overall system, B.) ClO_4^- anion, and C.) Ni metal. The lines illustrate the s-orbital (blue), p-orbital (red), and d-orbital (green) characteristics of the atoms within the crystal.

either of these contributions can dominate depending on the type of material, defects, and temperature. In our calculations using the current methodology, we can gather information only about the electronic part of the material. The fact that the material with a larger band gap exhibits higher conductivity could be due to the dominance of the ionic behavior of the material, directly related to the presence of anions in the structure.

CONCLUDING REMARKS

In this study, we have successfully synthesized and crystallographically characterized two Ni(II) complexes derived from a newly synthesized heterocyclic ligand ($\mathbf{N_3L_1}$) having different counteranions, showcasing their ability to form various supramolecular architectures. The coordination environment around each Ni(II) is distorted octahedral employing two pyrazinyl and one pyridyl nitrogen atom from each ligand moieties. We have demonstrated an orchestrated interplay among $\pi\cdots\pi$, anion$\cdots\pi$, and hydrogen bonding interactions that can lead to a strong cooperative/synergistic effect. Detailed X-ray crystallographic analysis reveals that though both complexes bear almost similar crystallographic parameters depending upon the nature and orientation of counterions, and they exhibit unique structural and interactional motifs. A DFT study was used to evaluate the synergistic influence of all possible types of anion$\cdots\pi$ and hydrogen bonding interactions. Furthermore, the theoretical study extends to rationalize the electrical properties of these complexes, highlighting their potential in electronic device applications, particularly in efficient Schottky diodes, as evident from the experimental investigation. Theoretical studies clearly established the semiconducting nature of both the complexes and a decisive role of anions. Complex **2**, with perchlorate anions, demonstrated superior electronic properties, attributed to its more favorable and stronger anion$\cdots\pi$ interactions and overall structural arrangement than that of complex **1**. These findings not only enrich our understanding of the influence of anionic components in supramolecular architectures but also pave the way for the design of new materials with tailored properties for specific technological applications.

ASSOCIATED CONTENT

Supporting Information

The Supporting Information is available free of charge at https://pubs.acs.org/doi/10.1021/acsomega.4c06270.

X-ray data for complex **1** (CIF)

https://doi.org/10.1021/acsomega.4c06270
ACS Omega 2024, 9, 44494−44506

X-ray data for complex **2** (CIF)

Synthetic schemes; spectral data (^{1}H NMR, ^{13}C NMR, FTIR, HRMS); crystal data table; hydrogen-bonding parameters; geometrical parameters for $\pi\cdots\pi$, anion$\cdots\pi$ interactions; supramolecular assemblies; optical characterization; device fabrication; device parameters (PDF)

AUTHOR INFORMATION

Corresponding Authors

Antonio Frontera − *Departament de Química, Universitat de les Illes Balears, 07122 Palma de Mallorca, Spain;* orcid.org/0000-0001-7840-2139; Email: toni.frontera@uib.es

Subrata Mukhopadhyay − *Department of Chemistry, Jadavpur University, Kolkata 700032, India;* orcid.org/0000-0001-7993-7426; Email: ju_subrata@yahoo.co.in

Authors

Subhajit Saha − *Department of Chemistry, Jadavpur University, Kolkata 700032, India*

Samit Pramanik − *Department of Chemistry, Jadavpur University, Kolkata 700032, India*

Sudipta Pathak − *Department of Chemistry, Haldia Government College, Debhog, West Bengal 721657, India*

Kinsuk Das − *Department of Chemistry, Chandernagore College, Hooghly, West Bengal 712136, India;* orcid.org/0000-0002-7717-8734

Riya Sadhukhan − *Organic Electronics Laboratory, Department of Physics, Indian Institute of Technology Kharagpur, Kharagpur 721302, India*

Arnab Ghosh − *Department of Physics and Natural Science Research Centre of Belda College under Vidyasagar University, Belda, West Bengal 721424, India;* orcid.org/0000-0003-1828-9837

Dipak K. Goswami − *Organic Electronics Laboratory, Department of Physics, Indian Institute of Technology Kharagpur, Kharagpur 721302, India;* orcid.org/0000-0002-5891-6172

Hon Man Lee − *Department of Chemistry, National Changhua University of Education, Changhua 50058, Taiwan;* orcid.org/0000-0002-9557-3914

Joaquín Ortega-Castro − *Departament de Química, Universitat de les Illes Balears, 07122 Palma de Mallorca, Spain;* orcid.org/0000-0001-8131-0315

Complete contact information is available at: https://pubs.acs.org/10.1021/acsomega.4c06270

Notes

The authors declare no competing financial interest.

ACKNOWLEDGMENTS

S.S. is thankful to University Grants Commission (New Delhi), for providing a Junior Research Fellowship. Thanks to the MICIU/AEI of Spain (project PID2020-115637GB-I00, FEDER funds) for financial support. We thank the CTI (UIB) for computational facilities.

REFERENCES

(1) Akhtaruzzaman; Khan, S.; Dutta, B.; Kannan, T. S.; Kumar Kole, G.; Hedayetullah Mir, M. Cocrystalsfor Photochemical Solid-State Reactions: An Account on Crystal Engineering Perspective. *Coord. Chem. Rev.* **2023**, *483*, 215095−215138.

(2) Li, H. Y.; Zhao, S. N.; Zang, S. Q.; Li, J. Functional Metal−Organic Frameworks as Effective Sensors of Gases and Volatile Compounds. *Chem. Soc. Rev.* **2020**, *49*, 6364−6401.

(3) Sun, Q.; Qin, L.; Lai, C.; Liu, S.; Chen, W.; Xu, F.; Ma, D.; Li, Y.; Qian, S.; Chen, Z.; Chen, W.; Ye, H. Constructing Functional Metal-Organic Frameworks by Ligand Design for Environmental Applications. *J. Hazard. Mater.* **2023**, *447*, 130848−130868.

(4) Lustig, W. P.; Mukherjee, S.; Rudd, N. D.; Desai, A. V.; Li, J.; Ghosh, S. K. Metal−Organic Frameworks: Functional Luminescent and Photonic Materials for Sensing Applications. *Chem. Soc. Rev.* **2017**, *46*, 3242−3285.

(5) Yu, M. H.; Liu, X. T.; Space, B.; Chang, Z.; Bu, X. H. Metal-Organic Materials with Triazine-Based Ligands: From Structures to Properties and Applications. *Coord. Chem. Rev.* **2021**, *427*, 213518−213562.

(6) Desiraju, G. R. Crystal Engineering: A Holistic View. *Angew. Chem., Int. Ed.* **2007**, *46*, 8342−8356.

(7) Nangia, A. K.; Desiraju, G. R. Crystal Engineering: An Outlook for the Future. *Ang Angew. Chem. Int. Ed.* **2019**, *58*, 4100−4107.

(8) Savastano, M.; Lopez de la Torre, M. D.; Pagliai, M.; Poggi, G.; Ridi, F.; Bazzicalupi, C.; Melguizo, M.; Bianchi, A. Crystal Engineering of High Explosives Through Lone Pair-π Interactions: Insights for Improving Thermal Safety. *iScience* **2023**, *26*, No. 107330.

(9) Pal, P.; Das, K.; Hossain, A.; Frontera, A.; Mukhopadhyay, S. Supramolecular and Theoretical Perspectives of2,2′:6′,2″-Terpyridine Based Ni(II) and Cu(II) Complexes: On the Importance of C−H$\cdots$Cl and $\pi\cdots\pi$ Interactions. *New J. Chem.* **2020**, *44*, 7310−7318.

(10) Haque, A.; Alenezi, K. M.; Khan, M. S.; Wong, W. Y.; Raithby, P. R. Non- Covalent Interactions (Ncis) in π-Conjugated Functional Materials: Advances and Perspectives. *Chem. Soc. Rev.* **2023**, *52*, 454−472.

(11) Li, S.; Xu, Y.; Shen, Q.; Liu, X.; Lu, J.; Chen, Y.; Lu, T.; Luo, C.; Luo, X.; Zheng, M.; Jiang, H. Non-Covalent Interactions with Aromatic Rings: Current Understanding and Implications for Rational Drug Design. *Curr. Pharm. Des.* **2013**, *19*, 6522−6533.

(12) Pramanik, S.; Pathak, S.; Frontera, A.; Mukhopadhyay, S. Syntheses, Crystal Structures and Supramolecular Assemblies of Two Cu (II) Complexes Based on a New Heterocyclic Ligand: Insights into C−H$\cdots$Cl and $\pi\cdots\pi$ Interactions. *CrystEngComm.* **2022**, *24*, 1598−1611.

(13) Li, J.; Feng, Q.; Wang, C.; Mo, Y. On the Nature of Inter-Anion Coinage Bonds. *Phys. Chem. Chem. Phys.* **2023**, *25*, 15371−15381.

(14) Pal, P.; Das, K.; Hossain, A.; Gomila, R. M.; Frontera, A.; Mukhopadhyay, S. Synthesis and Crystal Structure of the Simultaneous Binding of Ni(II) Cation and Chloride by the Protonated 2, 4, 6 tris-(2-pyridyl)-1, 3, 5 triazine Ligand: Theoretical Investigations of Anion$\cdots\pi$, $\pi\cdots\pi$ and Hydrogen Bonding Interactions. *New J. Chem.* **2021**, *45*, 11689−11696.

(15) Pramanik, S.; Hossain, A.; Pathak, S.; Ghosh Chowdhury, S.; Karmakar, P.; Frontera, A.; Mukhopadhyay, S. Revealing the Supramolecular Features of Two Zn (II) Complexes Derived from a New Hydrazone Ligand: A Combined Crystallographic, Theoretical and Antibacterial Study. *CrystEngComm.* **2023**, *25*, 866−876.

(16) Li, L.; Zhang, Y. Z.; Yang, C.; Liu, E.; Golen, J. A.; Zhang, G. One- Dimensional Copper (II) Coordination Polymers Built on 4′-substituted 4, 2′: 6′,4 ″- and 3,2′:6′,3″-terpyridines: Syntheses, Structures and Catalytic Properties. *Polyhedron.* **2016**, *105*, 115−122.

(17) Wei, C.; He, Y.; Shi, X.; Song, Z. Terpyridine-Metal Complexes: Applications in Catalysis and Supramolecular Chemistry. *Coord. Chem. Rev.* **2019**, *385*, 1−19.

(18) Schubert, U. S.; Eschbaumer, C. MacromoleculesContaining Bipyridine and Terpyridine Metal Complexes: Towards Metallosupramolecular Polymers. *Angew. Chem., Int. Ed.* **2002**, *41*, 2892−2926.

(19) Wang, S.; Chu, W.; Wang, Y.; Liu, S.; Zhang, J.; Li, S.; Wei, H.; Zhou, G.; Qin, X. Synthesis, Characterization and Cytotoxicity of Pt(II), Pd(II), Cu(II) and Zn(II) Complexes with 4′-Substituted Terpyridine. *Appl. Organomet. Chem.* **2013**, *27*, 373−379.

https://doi.org/10.1021/acsomega.4c06270
ACS Omega 2024, 9, 44494−44506

(20) Naseri, Z.; Nemati Kharat, A.; Banavand, A.; Bakhoda, A.; Foroutannejad, S. First Row Transition Metal Complexes of Thienyl Substituted Terpyridine: Structural, Photophysical and Biological Studies. *Polyhedron.* **2012**, *33*, 396−403.
(21) Mughal, E. U.; Mirzaei, M.; Sadiq, A.; Fatima, S.; Naseem, A.; Naeem, N.; Fatima, N.; Kausar, S.; Altaf, A. A.; Zafar, M. N.; Khan, B. A. Terpyridine- Metal Complexes: Effects of Different Substituents on their Physico- Chemical Properties and Density Functional Theory Studies. *R. Soc. Open Sci.* **2020**, *7*, 201208.
(22) Lo, K. K. W. Luminescent Rhenium (I) and Iridium (III) Polypyridine Complexes as Biological Probes, Imaging Reagents, and Photocytotoxic Agents. *Acc. Chem. Res.* **2015**, *48*, 2985−2995.
(23) Adeloye, A. O.; Ajibade, P. A. Towards the Development of Functionalized Polypyridine Ligands for Ru (II) Complexes as Photosensitizers in Dye- Sensitized Solar Cells (DSSCs). *Molecules.* **2014**, *19*, 12421−12460.
(24) Dalton, H. L.; Hawes, C. S.; Gunnlaugsson, T. Crystal Engineering of 6-carboxy-4-aryl-2,2′-bipyridine Complexes: Potent Chelators with Intrinsic Intermolecular Affinity. *Cryst. Growth Des.* **2017**, *17*, 4365−4376.
(25) Winter, A.; Schubert, U. S. Metal-Terpyridine Complexes in Catalytic Application−A Spotlight on the Last Decade. *ChemCatChem.* **2020**, *12*, 2890−2941.
(26) Schubert, U. S.; Winter, A.; Newkome, G. R. *Terpyridine-Based Materials: for Catalytic, Optoelectronic and Life Science Applications.*; John Wiley & Sons, 2012.
(27) Zhao, F. J.; Wang, H.; Li, K.; Wang, X. D.; Zhang, N.; Zhu, X.; Zhang, W.; Wang, M.; Hao, X. Q.; Song, M. P.; Li, X. Ditopic Chiral Pineno-Fused 2,2′:6′,2″-terpyridine: Synthesis, Self-Assembly, and Optical Properties. *Inorg. Chem.* **2019**, *58*, 15039−15044.
(28) Yam, V. W. W.; Wong, K. M. C. Luminescent Metal Complexes of d^6, d^8 and d^{10}Transition Metal Centres. *ChemComm.* **2011**, *47*, 11579−11592.
(29) Ghosh, A.; Guha, P.; Mukherjee, S.; Bar, R.; Ray, S. K.; Satyam, P. V. Growth of Au Capped GeO_2 Nanowires for Visible-Light Photodetection. *Appl. Phys. Lett.* **2016**, *109*, No. 123105.
(30) Sze, S. M. *Physics of Semiconductor Devices.*; Wiley: New York, 1969; p 496.
(31) Rhoderick, E. H.; Williams, R. H. *Metal-Semiconductor Contacts*; Clarendon Press: Oxford, 1988.
(32) Cheung, S. K.; Cheung, N. W. Extraction of Schottky Diode Parameters from forward Current-Voltage Characteristics. *Appl. Phys. Lett.* **1986**, *49*, 85−87.
(33) Allen, M. W.; Durbin, S. M.Influence of Oxygen Vacancies on Schottky Contacts to ZnO. *Appl. Phys. Lett.* **2008**, *92*, 12110−12113.
(34) Dang Tran Quan; Hbib, H. High Barrier Height Au/n-Type InP Schottky Contacts with a $PO_xN_yH_z$ Interfacial Layer. *Solid-State Electron.* **1993**, *36*, 339−344.
(35) Campos, M; Bulhoes, L.O.S; Lindino, C. A Gas-Sensitive Characteristics ofMetal/Semiconductor Polymer Schottky Device. *Sens. Actuators A Phys.* **2000**, *87*, 67−71.
(36) Das, D.; Das, M.; Sahu, P.; Pratim Ray, P.; Investigation of the Metal- Semiconductor Interface by Equivalent Circuit Model in Zinc Phthalocyanine (Znpc) Based Schottky Diodes and its Charge Transport Properties, *Mater. Today.* **2023**, DOI: 10.1016/j.matpr.2023.04.274.
(37) Pramanik, S.; Pathak, S.; Jana, S.; Mondal, M.; Frontera, A.; Mukhopadhyay, S. An Experimental and Theoretical Exploration of Supramolecular Interactions and Photoresponse Properties of Two Ni(II) Complexes. *New J. Chem.* **2021**, *45*, 12108−12119.
(38) Pramanik, S.; Jana, S.; Das, K.; Pathak, S.; Ortega-Castro, J.; Frontera, A.; Mukhopadhyay, S. Crystallographic Aspects, Photophysical Properties, and Theoretical Survey of Tetrachlorometallates of Group 12 Metals [Zn(II), Cd(II), and Hg(II)] with a Triply Protonated 2, 4, 6-tris (2-pyridyl)-1, 3, 5- triazine Ligand. *Inorg. Chem.* **2023**, *62*, 7220−7234.
(39) Sun, L.; Shu, S.; Zhou, Y.; Hou, S.; Liu, Y.; Ke, Z. Regulating the Optoelectronic Properties of Nickel Dithiolene by the Substituents: a Theoretical Study. *Materials.* **2018**, *11*, 2192.
(40) Perdew, J. P.; Levy, M. Physical Content of the Exact Kohn-Sham Orbital Energies: Band Gaps and Derivative Discontinuities. *Phys. Rev. Lett.* **1983**, *51*, 1884−1887.

https://doi.org/10.1021/acsomega.4c06270
ACS Omega 2024, 9, 44494−44506